Published in final edited form as:
Med Phys. 2007 March ; 34(3): 1026–1036.

Monte Carlo simulations of absorbed dose in a mouse phantom from 18-fluorine compounds

Richard Taschereau and **Arion F. Chatziioannou**
The Crump Institute for Molecular Imaging, Department of Molecular and Medical Pharmacology, David Geffen School of Medicine at UCLA, 700 Westwood Boulevard, Los Angeles, California 90095

Abstract

The purpose of this study was to calculate internal absorbed dose distribution in mice from preclinical small animal PET imaging procedures with fluorine-18 labeled compounds (^{18}FDG, ^{18}FLT, and fluoride ion). The GATE Monte Carlo software and a realistic, voxel-based mouse phantom that included a subcutaneous tumor were used to perform simulations. Discretized time-activity curves obtained from dynamic *in vivo* studies with each of the compounds were used to set the activity concentration in the simulations. For ^{18}FDG, a realistic range of uptake ratios was considered for the heart and tumor. For each simulated time frame, the biodistribution of the radionuclide in the phantom was considered constant, and a sufficient number of decays were simulated to achieve low statistical uncertainty. Absorbed dose, which was scaled to take into account radioactive decay, integration with time, and changes in biological distribution was reported in mGy per MBq of administered activity for several organs and uptake scenarios. The mean absorbed dose ranged from a few mGy/MBq to hundreds of mGy/MBq. Major organs receive an absorbed dose in a range for which biological effects have been reported. The effects on a given investigation are hard to predict; however, investigators should be aware of potential perturbations especially when the studied organ receives high absorbed dose and when longitudinal imaging protocols are considered.

Keywords

small animal PET; dosimetry; GATE; Flourine-18

I. INTRODUCTION

Positron emission tomography (PET) is used in the study of biological processes[1] both in humans and small animals, in cancer research,[2–4] gene therapy,[5] investigation on myocardium pathology,[6,7] and brain imaging.[8,9] In preclinical small animal studies, there is some concern about the radiation absorbed dose delivered to the subject especially in the case of longitudinal studies and when PET is combined with small animal computed tomography (microCT).[10–12] However, the absorbed dose distribution in the animal from compounds used in PET is not well characterized. Most studies published on internal radiation absorbed dose were performed in the context of therapeutic radiopharmaceuticals,[13,14] not imaging compounds. Very few studies have investigated the dosimetric aspect of PET imaging on small animals, though they seem to indicate that the radiation dose may be non-negligible. Funk *et al.*[15] have used the Monte Carlo method and the MIRD methodology[16,17] to calculate absorbed dose in a homogeneous, geometrical phantom from a point source and uniformly distributed source. Such a study can provide good whole-body absorbed dose estimates. However, due to the small size of the organs and structures involved and since dose is mainly delivered from short-range positrons, a more detailed,

finer-resolution investigation is needed in order to assess the absorbed dose spatial distribution.

In previous work, we have reported on the absorbed dose to small animals[18] from x-ray microCT procedures. Here, we report on the absorbed dose from PET procedures using common fluorine-18 compounds: [(18)F]fluoro-D-glucose (^{18}FDG) used for metabolism studies,[19–21] 3′-deoxy-3′-[(18)F]fluorothymidine (^{18}FLT) used in cell proliferation investigations,[22–24] and [(18)F]fluoride ion used for bone turnover studies.[25,26]

Time-activity curves were extracted from mouse studies and activity was transposed in an anatomically realistic mouse phantom.[27] The mouse phantom contained 25 important organs/structures such as bones, liver, heart, bladder, etc. The Monte Carlo method was used to calculate absorbed dose distributions to sensitive organs. Although more computationally intensive, the Monte Carlo method has been preferred over other methods, such as convolution with a dose kernel, because it takes into account the inhomogeneities (air cavities, lungs, bones, fat) and distant energy deposition all at once. For convenience, absorbed dose normalized to the amount of administered activity is presented in tables and in the form of dose-volume histograms.

II. MATERIALS AND METHODS

A. Data acquisition

1. PET studies—Three studies using different fluorine-18 compounds (^{18}FDG, ^{18}FLT, and fluoride ion) were conducted on mice anesthetized with isoflurane using a microPET® Focus™ 220 tomograph (Siemens Preclinical Solutions, Knoxville, TN), acquiring listmode data from the time of tracer injection into the tail vein, up to 90 min later. The data were subsequently grouped into a number of dynamic frames depending on tracer kinetics, corrected for photon scatter and attenuation, and reconstructed using the filtered back projection (FBP) algorithm. For ^{18}FDG, 24 MBq were administered and 90 min of acquired data were divided into 34 temporal frames; for FLT, 9.1 MBq were administered and 60 min of acquired data were divided into 19 frames; finally for fluoride ion, 9.8 MBq were administered and 60 min of acquired data were divided into 19 frames. For the fluorine ion study, the small spatial scale associated with mouse bone uptake required a higher spatial resolution, and the maximum *a posteriori* probability (MAP) reconstruction algorithm was also used.[28]

2. Tracer uptake—The tracer uptake for different organs was calculated for all studies via three-dimensional regions of interest (ROIs) on the reconstructed images from the dynamic data. Uptake was characterized in one of two ways: fractional time-activity curves $f_h(t)$ or standardized uptake values (SUV), defined as[29]

$$\mathrm{SUV}(t)=\frac{A_h(t)/V_h}{A_0/M_T}(\mathrm{g/mL}), \tag{1}$$

where A_h and V_h are organ activity and volume, respectively, A_0 is the administered activity, and M_T is the subject mass. It is clear from Eq. (1) that fractional activity $f_h(t)=A_h(t)/A_0$ can be converted to SUV and vice versa provided V_h and M_T are known:

$$f_h(t)=\mathrm{SUV}(t)\cdot\frac{V_h}{M_T}. \tag{2}$$

In this study fractional activity has been used as input to the simulation program, while the SUV has been used for establishing different imaging scenarios and reporting results.

To extract time activity curves, regions of interest were first identified in reconstructed PET images using various 3D visualization software (Amide,[30] Amira 3.0, Mercury Computer Systems, San Diego, CA). ROIs were drawn over time-integrated PET images (i.e., activity images representing the total duration of the study), which were preferred over microCT scans in order to eliminate the effects of possible organ motion and, in the case of the bladder, organ expansion. For organs with a simple shape (e.g., bladder, tumor), ROIs were drawn using a geometric form (e.g., ellipsoid). For more complex shapes (e.g., kidneys, heart) the smallest iso-activity surface encompassing the organ was used. Once an ROI was defined, it was used to collect activity for all time frames of the study. To illustrate the procedure, Fig. 1(a) shows the 90 min time-integrated image (coronal and sagittal views) for the FDG study with a 3D ellipsoid ROI drawn around the bladder. Figure 1(b) shows the bladder ROI superimposed on selected frames as time increases and activity $A_h(t)$ accumulates in the bladder. Care was taken so that regions were mutually exclusive (e.g., bladder activity was not counted in body activity). Identified organs and structures of interest were bladder, kidneys, liver, tumor, heart, body as a whole for ^{18}FDG; bladder, tumor, guts, body as a whole for ^{18}FLT; bladder, kidneys, bones, spine, body as a whole for fluoride ion. The activity A_h in each region from each time frame was extracted and normalized to the administered activity A_0. For ^{18}FLT and fluoride ion, these time-activity curves were considered representative of typical studies. A complete list of organs is given in Tables I and II.

^{18}FDG was treated differently. It has been shown[31] that with ^{18}FDG, tracer uptake exhibits variability, especially for the heart and tumor. In order to provide more general results, a range of end-of-scan SUVs for the heart and tumor from Ref. [31] were used: for the heart, SUV was taken to be in the range of 0 to 8 g/mL and, for the tumor, SUV was in the range of 0 to 2 g/mL. A zero SUV value, although experimentally not realized, was also considered because of its usefulness in establishing a relationship with absorbed dose. A number of scenarios were devised and labeled H*x*T*y* where H*x* was the heart SUV value and T*y* was the tumor SUV value, ranging from 0 to 8 and from 0 to 2, respectively. For simulations, SUVs for the heart and tumor were converted to time-activity curves using Eq. (2) and combined with time-activity curves from measured data for the rest of the organs (bladder, liver, kidneys and whole body). A long biological half-life was assumed so that tracer clearance from organs was neglected. As an example, Fig. 2 shows normalized time-activity curves for ^{18}FDG (H4T1 scenario), ^{18}FLT (H1T4.7) and fluoride ion.

B. Monte Carlo environment

1. Software—The GATE Monte Carlo software32 was used to perform all simulations. This software was initially developed for SPECT and PET scanner development and investigations but a new feature available in the latest GATE version allows for absorbed dose map calculations from voxel-based phantoms. GATE is based on the GEANT4 toolkit, 33 a well established code for radiation transport. The GATE/GEANT4 package comes with an all-purpose set of physics processes valid for a wide range of energies but also offers alternative options. In this study, a special set of electromagnetic processes (the PENELOPE option) was used for the transport of electrons and positrons. The PENELOPE option implements the same physics as the PENELOPE software[34] and extends the validity range of particle interactions to lower energies (a few hundred eV to about 1 GeV). Fluorine-18 is a proton-rich radionuclide decaying by electron capture (3.27%) or positron emission (96.73%) to a stable isotope of oxygen with a half-life of 109.77 minutes. The positron energy follows a Fermi distribution with an average of 242.8 keV and a maximum of 633.5

keV. Fluorine decay was simulated by isotropically emitting positrons each having an initial energy chosen according to the ^{18}F positron energy spectrum. Positrons were tracked until they annihilated, at which point annihilation photons were emitted and tracked. Since not every radionuclide decay results in positron emission, dose calculations were corrected for positron yield by multipliying by 0.9673, the branching ratio for positron emission.

2. Digital mouse phantoms—Four different anatomically realistic mouse phantoms were used for this study, each phantom providing focus on a different aspect of dosimetry. The first phantom was an enhanced low-resolution (400 μm)^3 version of the MOBY whole-body mouse phantom[27] representing a 33 g, normal 16-week-old male C57B1/6 mouse. The phantom, shown in Fig. 3(a), was first realized as a three-dimensional, rectangular array of cubic voxels. It was enhanced by the addition of missing anatomical structures (skin, bladder wall, and bone marrow), the segregation of bone types (cranium, ribs, spine, and lower limbs) and air- or liquid-containing organs (lungs, trachea, intestines), and the assignment of tissue properties based on human counterparts.[35] This whole-mouse phantom was used for the fluoride ion experiments. In the case of ^{18}FDG and ^{18}FLT, a 7 mm diameter spherical tumor was also added in the axillary area. A resolution of 400 μm was adequate for most organs, however higher spatial resolution was required to render the fine structure of bone and marrow, and also for the bladder wall.

A second phantom composed from the bladder only was used for bladder wall dosimetry. It was a high-resolution phantom (50 μm)^3 created from MOBY by zooming on the bladder region and is shown in Fig. 3(b). Activity was placed only inside the bladder, assuming that a very high SUV makes the absorbed dose contribution from outside elements negligible. The wall thickness varied from 440 to 480 μm, based on MOBY. The third and fourth phantoms were especially created for bone marrow dosimetry: one represented a section of the femur head [Fig. 3(c)] and one represented a vertebra [Fig. 3(d)]. The femur section was a high-resolution phantom (15 μm)^3 created by replicating a segmented, two-dimensional image of a cross section of a bone[18] to form a 3D structure. It contained four regions: soft tissue, cortical and trabecular bone, and marrow. The vertebra phantom (25 μm)^3 was created by segmenting slices of the microCT images acquired along with PET scans required by this study. This vertebra phantom contained bone and bone marrow and was surrounded by soft tissue and air. For all bone phantoms, activity was placed on bone surfaces, both inside and outside.

3. Simulation setup—Time-activity curves (from PET studies and converted SUV values) were resampled at selected time points using cubic-spline interpolation. Time points were initially chosen at approximately equidistant logarithmic intervals at a rate of about 3 points per decade (e.g., 1, 2, 5, 10 min, etc). They were later adjusted to the kinetics of the tracer and also to match the duration of the study (60 or 90 min). Resampled curves were used to establish bio-distributions of each tracer in the phantom. For each time point, a simulation was performed with the corresponding bio-distribution, which was considered fixed for the duration of the time frame. Depending on phantom size and resolution, a nominal activity in the range 20 to 100 MBq was assigned to each frame, for the duration of one virtual second. This was a compromise between required computation time and uncertainty on calculated absorbed dose, which was kept under 5% for 95% of all voxels. Simulations were run on a cluster of 24 dual 3.2-GHz xeon processors and required about 330 h of processor time per time frame for a grand total of about 10 000 h for all simulations.

4. Absorbed dose calculations—The simulation output was volumetric absorbed dose maps with the same dimensions as the phantom, i.e., absorbed dose was calculated at the voxel level with one complete absorbed dose matrix per time frame. The raw data were

scaled for the actual scan duration and activity and combined to arrive to the final absorbed dose.

For the whole-mouse phantom, the following calculations were performed. Let $\dot{D}_k(x, y, z, t)$ be the absorbed dose rate at time t at point (x, y, z) corresponding to a static bio-distribution of the tracer identified by the subscript k. The absorbed dose per unit administered activity at a given point $D_k(x, y, z)/A_0$ received during a time period starting at time t_k, corresponding to the static bio-distribution k and of duration Δt_k, is obtained by integration of the absorbed dose rate:

$$\begin{aligned}\frac{D_k(x,y,z)}{A_0} &= \frac{1}{A_0}\int_{t_k}^{t_k+\Delta t_k}\dot{D}_k(x,y,z,t)dt \\ &= \frac{\dot{D}_k(x,y,z,t=0)}{A_0}\int_{t_k}^{t_k+\Delta t_k}e^{-\lambda t}dt \\ &= \frac{\dot{D}_k(x,y,z,t=0)}{A_0}f_k,\end{aligned} \tag{3}$$

where λ is the radionuclide decay constant and f_k is the time-frame decay factor (the value of the integral) having dimensions of time. As a result of choosing a simulated duration of 1 s and the same nominal activity for every frame (e.g., A_0=100 MBq), each absorbed dose matrix M_k corresponding to bio-distribution k could be interpreted as the absorbed dose rate at time t=0, $\dot{D}_k(x, y, z, t=0)$ for that nominal activity and bio-distribution. Substituting M_k in place of $\dot{D}_k(x, y, z, t=0)$ in Eq. (3) and summing over all time frames, one obtains the cumulative absorbed dose (identified by a tilde) per unit administered activity:

$$\frac{\tilde{D}}{A_0}=\sum_k\frac{D_k}{A_0}=\sum_k\frac{M_k}{A_0}f_k. \tag{4}$$

Dose-volume histograms and absorbed dose averages were subsequently calculated for each organ in the phantom.

For high-resolution phantoms, representing isolated parts of the body—as opposed to the body as a whole—the use of time-activity curves was not necessary since absorbed dose could be calculated by scaling with a time equivalent factor. For the bladder wall, the cumulative absorbed dose per unit administered activity at high resolution $\tilde{D}_{high}/A_0$ was obtained by multiplying the dose rate per unit activity in the bladder with a time equivalent factor T_{equ}:

$$\frac{\tilde{D}_{high}}{A_0}=T_{equ}\left[\frac{D_{sim}/T_{sim}}{A_{blad}}\right]_{high}, \tag{5}$$

where D_{sim} was the calculated (simulated) absorbed dose to the bladder wall, and A_{blad} and T_{sim} were the simulated activity in the bladder and duration, respectively. The time equivalent factor was calculated from the low-resolution whole-mouse phantom by dividing the cumulative absorbed dose to the bladder $[\tilde{D}/A_{blad}]_{low}$(per unit activity in the bladder) by the end-of-scan dose rate to the bladder (per unit activity in the bladder):

$$T_{equ}=\left[\frac{\tilde{D}}{A_{blad}}\right]_{low}\left[\frac{D_{sim}T_{sim}}{A_{blad}}\right]_{low}^{-1}. \tag{6}$$

Thus, T_{equ} translates the effects of activity redistribution from the low-resolution to the high-resolution phantom. The subscripts *high* and *low* in Eqs. (5) and (6) refer to the high- and low-resolution phantoms, respectively. For bone marrow phantoms (vertebra and femur head), the cumulative absorbed dose per unit administered activity $\tilde{D}/A_0$ was calculated as follows:

$$\frac{\tilde{D}}{A_0}=\left(\frac{D_{sim}/T_{sim}}{A_{bone}^{Phantom}/L_{bone}^{Phantom}}\right)\left(\frac{A_{bone}^{PET}}{L_{bone}^{PET}}\right)T_{equ}\frac{1}{A_0}, \tag{7}$$

where D_{sim}, T_{sim} and T_{equ} have the same meaning as before, and where $A_{bone}^{Phantom}$ was the activity in the bone phantom, A_{bone}^{PET} was the end-of-scan activity in bone from PET, A_0 was the administered activity, $L_{bone}^{Phantom}$ was the length of the bone phantom, and L_{bone}^{PET} was the length of bone in PET.

The first factor in Eq. (7) is the result of simulations and is the absorbed dose rate per unit activity per unit bone length in the bone phantom; the second factor is the activity per unit bone length in real bone from the PET image; the third factor is the time-equivalent factor and finally A_0 is the administered activity. For these phantoms, time equivalent factors were calculated by dividing the cumulative absorbed dose in bone (per unit activity in bone) by the end-of-scan dose rate in bone (per unit activity in bone), both values taken from the low-resolution calculations.

Since absorbed dose to the bone marrow was calculated using two different phantoms of different resolution, representing different parts of the body (femur and vertebra), a method had to be developed to combine results to produce a joint bone marrow dose-volume histogram. First, individual normalized dose-volume density histograms H_n were calculated for each phantom. For each voxel in the phantom, the absorbed dose was tallied using the following formula:

$$H_n(D_i) \leftarrow H_n(D_i)+\frac{1}{N_n\Delta D}, \tag{8}$$

where ΔD is the histogram dose-bin width, N_n is the number of voxels in phantom n, D_i is the absorbed dose in the voxel collected from phantom n, $H_n(D_i)$ is the dose-bin in histogram H_n corresponding to dose D_i, and the left arrow is an assignment operator. Histograms were then added to produce a joint histogram:

$$H(D_i)=\sum_n w_n H_n(D_i) \quad \text{with} \sum_n w_n=1, \tag{9}$$

where w_n are weights representing the fraction of marrow in each phantom. Those weights, estimated from microCT scans, were 0.1 and 0.9 for the trabecular phantom and vertebra phantom, respectively.

5. Verification—A thorough validation of the positron tracking ability of GATE/GEANT was beyond the scope of this study. However, in order to avoid obvious errors, the behavior of the simulation software in tracking positrons was verified by reproducing a simulation by Levin and Hoffman[36,37] and comparing with their data. The simulation consisted in the emission of ^{18}F positrons in water and the calculation of the distribution of the x coordinate

of their annihilation endpoint. The data was histogrammed in 10 μm size bins. Raw data from Ref. [36] were not available; however the authors have fit a bi-exponential function, which was used for comparison. Results are plotted in Fig. 4 on a semi-logarithmic scale. There is overall good agreement between the histogram calculated with GATE and the fit obtained from Levin. At short distances, the agreement between the two is within a few percent. At larger distances the two curves depart from each other by about 20% at 1 mm and by a factor of 2 at 1.5 mm. Since Ref. [36] is not known to be a "gold standard," it was not possible to determine which curve was "right." However, it showed that there were no patent errors in the simulation environment.

III. RESULTS AND DISCUSSION

Results from calculations with all phantoms and tracers are summarized and presented in Table I. Each row gives absorbed dose for an organ or region of interest for each of the three tracers in normalized form, i.e., divided by the amount of administered activity (mGy/MBq). For the bladder wall, two rows are given: one for calculations with the whole-mouse phantom and one for the high-resolution phantom. For the heart and tumor, rather than a single value, a formula is given in Table I to calculate absorbed dose per unit activity as a function of SUV. Absorbed dose to bone marrow from fluoride ion and from low- and high-resolution phantoms is also presented on separate lines. By normalizing absorbed dose and using the SUV, Table I is meant to help investigators assess the absorbed dose per organ on any given procedure without requiring long and costly computer simulations.

Table II is similar to Table I, except that it shows an example of absolute absorbed dose calculated for an injection of 7.4 MBq, a typical amount of activity used by investigators at our institution. In Table II, SUVs of 4 and 2 g/mL were assumed for the heart and tumor, respectively, for ^{18}FDG dose calculations. The SUV for the tumor in the ^{18}FLT study was about 4.7 g/mL.

A. Heart and tumor

Figure 5 is a plot of normalized absorbed dose as a function of SUV for the heart and tumor calculated for an FDG bio-distribution. The near linearity of both relations is a consequence of the fact that, with a pure positron emitter like ^{18}F, absorbed dose to an organ is mainly due to activity and emission energy of positrons in that organ. Positrons' contribution to absorbed dose is local whereas annihilation photons' contribution is distant. The ordinate intercept at SUV=0 is the absorbed dose contribution from surrounding activity, when no activity is present in the organ. The heart intercept is slightly higher than that of the tumor (3.0 vs, 1.5 mGy/MBq) because of its central location in the body.

B. Bladder wall

The bladder wall was the structure that consistently received the highest absorbed dose, regardless of the tracer used. According to the low-resolution phantom (Table I, line 1) absorbed dose for the selected tracers was in the range of 340–540 mGy/MBq. Besides the physical explanation that activity eventually accumulates in the bladder, these high values were also due to the calculation method, which considered an unvoided bladder and integrated the absorbed dose rate for an infinite amount of time. It was observed however, that the cumulative absorbed dose at time t=90 min was only 38% (206 mGy/MBq) of the absorbed dose calculated over an infinite amount of time. This suggested that voiding the bladder—at least partially—could significantly reduce the cumulative absorbed dose.

Absorbed dose to the bladder wall can be estimated in a more realistic fashion using some mathematical model of bladder voidance. Multi-parameter analytical models have been

developed for humans[38] to estimate absorbed dose from activity. These models could not be applied integrally here since in this study absorbed dose has been calculated by explicit simulation and need not be estimated from activity and organ *S* values. However, the assumptions of these models can be used in devising a simple applicable model, which we describe below.

Let us begin with a first model we call the inelastic-bladder model. Assuming no tracer redistribution after 90 min, absorbed dose to the bladder wall can be calculated by interpolation using the two end values ($D_{(t=90)}$ and $D_{(t=\infty)}$) and the following expression:

$$D=D_{(t=90)}+(D_{(t=\infty)}-D_{(t=90)})[F(t_{void})+(1-g)(1-F(t_{void}))], \tag{10}$$

where t_{void} is the time (in excess of 90 min) when the bladder is voided, g is the fraction of bladder voiding (0: bladder full; 1: bladder empty), and $F(\cdot)$ is the cumulative exponential distribution function:

$$F(t)=\lambda\int_0^t e^{-\lambda\tilde{t}}d\tilde{t}, \tag{11}$$

with λ being the radionuclide decay constant. The main caveat of this inelastic model of bladder voidance is that it does not take into account changes in bladder size and shape or bladder wall thickness that occur as the bladder empties itself. In other words, the inelastic model assumes a direct proportionality between absorbed dose and activity, i.e., $D(A)=C_1A$, where C_1 is a constant. This also implies linearity: $D(kA)=kD(A)$.

Using an elastic bladder model, we make the assumptions that (a) the majority of positrons will be stopped within the bladder wall (nonpenetrating radiation) and (b) the total bladder activity is proportional to the organ volume: $A=C_2R_{in}^3$. Because of the short range of positrons, only positrons close to the wall will contribute to absorbed dose, hence absorbed dose to the bladder wall is proportional to its inner surface: $D=C_3R_{in}^2$. Combining the two previous expressions for activity and absorbed dose, one can write $D(A)=C_4A^{2/3}$. Absorbed dose is no longer directly proportional to activity (as with the inelastic model) but rather satisfies the following relation:

$$D(k\cdot A)=C_4(k\cdot A)^{2/3}=k^{2/3}C_4A^{2/3}=k^{2/3}D(A). \tag{12}$$

Equation (10) can be easily modified to include this nonlinearity since the factor $(1-g)$ is directly proportional to activity. By adding the exponent (2/3) to that factor we obtain

$$D=D_{(t=90)}+(D_{(t=\infty)}-D_{(t=90)})\cdot[F(t_{void})+(1-g)^{2/3}(1-f(t_{void}))]. \tag{13}$$

An isodose plot of Eq. (13) is shown in Fig. 6, using the time of voiding after administration (rather than in excess of 90 min) and absorbed dose taken from ^{18}FDG: $D_{(t=90)}$=206 mGy/MBq and $D_{(t=\infty)}$=543 mGy/MBq. It can be seen that voiding the bladder can reduce absorbed dose considerably. For example, 50% voiding occurring 135 min after injection reduces absorbed dose to 450 mGy/MBq (“A” label) and 80% voiding 90 min postinjection further reduces absorbed dose to 321 mGy/MBq (“B” label).

This level of absorbed dose (~500 mGy/MBq) may seem remarkably high, especially when compared to the 0.1–0.6 mGy/MBq reported for humans in MIRD Pamphlet 14.[38] However,

when normalized to activity per unit mass (as opposed to activity only), they become comparable.

Figure 7 shows dose-volume histograms of the bladder wall obtained with the whole-mouse phantom (low-resolution) and the high-resolution bladder phantom. The absorbed dose averages were 529 and 543 mGy/MBq for the high- and low-resolution phantoms, respectively, a difference of about 2.6%. This difference is mostly attributable to structural differences: the coarseness of the high-resolution phantom did not render subtleties of the wall contour as well as the high-resolution phantom. This factor of 2.6% was used to scale down all absorbed dose from the low-resolution phantom (line 1, Table I) to obtain values shown in line 2, Table I. The high-resolution distribution in Fig. 6 also exhibits a relatively longer tail, suggesting the presence of a steep dose gradient across the bladder wall. An absorbed dose profile across the wall (not shown) displayed a 75% drop in dose from the inside surface to the outside surface of the ~0.45 mm wall, confirming the presence of a strong gradient. The gradient was a consequence of the short distance (~1 mm) traveled by positrons in soft tissue. The highest absorbed dose was therefore received by the inner surface of the bladder.

C. Bone marrow

A bone marrow dose-volume histogram for fluoride ion is presented in Fig. 8. It shows results from the low-resolution whole-mouse phantom (dashed line) and a combination (solid line) of the two high-resolution bone phantoms (vertebra and femur head). Absorbed dose averages were 41 and 66 mGy/MBq for the low- and high-resolution phantoms, respectively. This important difference can be explained primarily by the fact that in the low-resolution phantom, marrow was only present in the spine. Therefore, the high activity present in bone joints did not contribute to the absorbed dose to the marrow in that phantom. There was, however, marrow in the femur head phantom to absorb energy from that activity. The distribution from the low-resolution phantom is also narrower, which is due to the larger voxel size having an averaging effect, which dampens out fluctuations around the average. The spread-out distribution in the high-resolution phantom is mainly due to the contribution of the femur phantom that adds a little hump centered at about 312 mGy/MBq.

Care must be taken in interpreting these results since they might not be directly applicable to a specific subject; they should rather be used as guidelines. In the past, investigators have used analytical approaches[39–41] (for humans) and voxelized representations of bone for dose calculations. However, bone has a complex geometry with an intricate mixture of spongiosa and marrow, which makes it difficult to model exactly and for which precise dose calculations may not be possible.

D. Other organs

Other organs showing relatively high absorbed dose, depending on the tracer, are the heart and kidneys for ^{18}FDG, bones and bone marrow for fluoride ion, and tumor for ^{18}FLT. It is of interest to compare these values with absorbed dose from microCT procedures. A typical microCT examination gives absorbed dose within the 70–90 mGy range for soft tissue and 250–400 mGy for bones.[18] A typical fluorine PET study uses 7.4 MBq of administered activity. From Table II, the heart in an FDG study would receive about five times the absorbed dose it would receive from microCT, and the kidneys more than twice as much. A fluoride ion scan would give an absorbed dose two and six times that of microCT for the spine and marrow, respectively.

A comparison was possible with another study that used ellipsoids, the MIRD methodology, and a different Monte Carlo code. According to Table IV in Ref. [15], the whole-body (source

and target identical) *S* value for a uniformly distributed ^{18}F source in a 30 g ellipsoid mouse is 15×10^{-13} Gy Bq^{-1} s^{-1}. Calculating the whole-body mean absorbed dose per unit activity using the MIRD formula,

$$D = S \int_0^\infty e^{-\lambda t} dt, \tag{14}$$

where λ is the radionuclide decay constant, one obtains 14.25 mGy/MBq, a value almost identical to the ones we report in Table I (third line) for ^{18}FDG and ^{18}FLT. The fluoride ion uptake is too localized to be compared to a uniformly distributed source like the one used in Ref. [15].

It is important to stress that the simulation experiments performed here were based on a few samples of *in vivo* studies that were considered typical and that the actual tracer bio-distribution is subject dependent and hence can be different than what shown here. Nevertheless, the data do demonstrate that radiation exposure is a significant caveat in small-animal imaging that cannot be neglected. Furthermore, our correlation of absorbed dose to SUV allows readers to obtain reasonable estimates for most scenarios in which the tracer is irreversibly bound or trapped.

The level of absorbed dose reported here is far from lethal; the LD50 for mice has been reported[42,43] to be between 6.5 and 7 Gy (whole body acute dose). Biological effects such as stimulated cell proliferation[44] and induced radio-resistance[45] have been observed for absorbed dose in the range of 50–500 mGy, although the mechanism through which this occurs is not totally understood. This study shows that organs like the bladder, heart, kidneys, thyroid, tumor, testes, pancreas, and brain can all receive absorbed dose in that range. The way this could affect any given investigation is hard to predict. However, investigators should be aware of potential interference especially when a high radiation dose is given to the organ or structure under investigation and when longitudinal studies are performed.

IV. CONCLUSION

A detailed investigation on radiation absorbed dose distribution from commonly used fluorine-18 compounds was performed using Monte Carlo simulations and a realistic mouse phantom. Depending on the tracer, relatively high doses can be given to the bladder wall, heart, kidneys, bones, bone marrow, and a tumor xenograft. Absorbed dose from microPET can be higher than absorbed dose from microCT by a large margin, depending on the organ, administered activity, and tracer used. While more work needs to be done with other radionuclides having different nuclear decay schemes and energy spectra, our method of SUV-based analysis for tumors simplifies approximate absorbed dose calculations for other imaging scenarios. These results could not have been inferred by using coarse approximations such as cylindrical phantoms or even *S* values and the MIRD methodology. Major organs receive an absorbed dose in a range for which biological effects have been reported. The effects on a given investigation are hard to predict; however, investigators should be aware of potential perturbations. In the case of the bladder wall, which is normally not the object of investigation nor a critical structure, the high absorbed dose it received warrants some precautions, especially in the case of longitudinal studies. Since it is relatively easy to reduce absorbed dose by partially voiding the bladder, this should become standard practice.

Acknowledgments

The authors wish to thank David Stout for scanner time and Judy Edwards and Waldemar Ladno for their assistance in performing scans. This work was supported in part by the U.S. Department of Energy under Contract No. DE-FC03-02ER63420 and by the National Institutes of Health under Grant No. R24 CA92865.

References

1. Phelps ME. Positron emission tomography provides molecular imaging of biological processes. Proc. Natl. Acad. Sci. U.S.A 2000;97:9226–9233. [PubMed: 10922074]
2. Kenanova V, et al. Tailoring the pharmacokinetics and positron emission tomography imaging properties of anti-carcinoembryonic antigen single-chain Fv-Fc antibody fragments. Cancer Res 2005;65:622–631. [PubMed: 15695407]
3. Abbey CK, Borowsky AD, McGoldrick ET, Gregg JP, Maglione JE, Cardiff RD, Cherry SR. In vivo positron of progression-emission tomography imaging of progression and transformation in model of mammary neoplasia. Proc. Natl. Acad. Sci. U.S.A 2004;101:11438–11443. [PubMed: 15277673]
4. Shu CYJ, Guo SL, Kim YJ, Shelly SM, Nijagal A, Ray P, Gambhir SS, Radu CG, Witte ON. Visualization of a primary anti-tumor immune response by positron emission tomography. Proc. Natl. Acad. Sci. U.S.A 2005;102:17412–17417. [PubMed: 16293690]
5. Rogers BE, Parry JJ, Andrews R, Cordopatis P, Nock BA, Maina T. MicroPET imaging of gene transfer with a somatostatin receptor-based reporter gene and Tc-94m-demotate 1. J. Nucl. Med 2005;46:1889–1897. [PubMed: 16269604]
6. Stegger L, Schafers KP, Flogel U, Livieratos L, Hermann S, Jacoby C, Keul P, Conway EM, Schober O, Schrader J, Levkau B, Schafers M. Monitoring left ventricular dilation in mice with PET. J. Nucl. Med 2005;46:1516–1521. [PubMed: 16157535]
7. Wu JC, Inubushi M, Sundaresan G, Schelbert HR, Gambhir SS. Positron emission tomography imaging of cardiac reporter gene expression in living rats. Circulation 2002;106:180–183. [PubMed: 12105155]
8. Vlassenko AG, Rundle MM, Raichle ME, Mintun MA. Regulation of blood flow in activated human brain by cytosolic NADH/NAD(+) ratio. Proc. Natl. Acad. Sci. U.S.A 2006;103:1964–1969. [PubMed: 16446430]
9. Kepe V, Barrio JR, Huang SC, Ercoli L, Siddarth P, Shoghi-Jadid K, Cole GM, Satyamurthy N, Cummings JL, Small GW, Phelps ME. Serotonin 1A receptors in the living brain of Alzheimer's disease patients. Proc. Natl. Acad. Sci. U.S.A 2006;103:702–707. [PubMed: 16407119]
10. Chow PL, Rannou FR, Chatziioannou AF. Attenuation correction for small animal PET tomographs. Phys. Med. Biol 2005;50:1837–1850. [PubMed: 15815099]
11. Chow PL, Rannou FR, Chatziioannou AF. Towards a beam hardening correction for a microCT scanner. Mol. Imaging Biol 2004;6:77–78.
12. Goertzen AL, Nagarkar V, Street RA, Paulus MJ, Boone JM, Cherry SR. A comparison of x-ray detectors for mouse CT imaging. Phys. Med. Biol 2004;49:5251–5265. [PubMed: 15656275]
13. Stabin MG, Peterson TE, Holburn GE, Emmons MA. Voxel-based mouse and rat models for internal dose calculations. J. Nucl. Med 2006;47:655–659. [PubMed: 16595500]
14. Kolbert KS, Watson T, Matei C, Xu S, Koutcher JA, Sgouros G. Murine S factors for liver, spleen, and kidney. J. Nucl. Med 2003;44:784–791. [PubMed: 12732681]
15. Funk T, Sun MS, Hasegawa BH. Radiation dose estimate in small animal SPECT and PET. Med. Phys 2004;31:2680–2686. [PubMed: 15487751]
16. Snyder, WS.; Ford, MR.; Warner, GG. Estimates of Specific Absorbed Fractions for Photon Sources Uniformly Distributed in Various Organs of a Heterogeneous Phantom. New York: MIRD; 1978. MIRD Pamphlet No. 5
17. Snyder, WS.; Ford, MR.; Warner, GG.; Watson, SB. Absorbed Dose per Unit Cumulated Activity for Selected Radionuclides and Organs. Reston, VA: MIRD; 1975. MIRD Pamphlet No. 11

18. Taschereau R, Chow PL, Chatziioannou AF. Monte Carlo simulations of dose from microCT imaging procedures in a realistic mouse phantom. Med. Phys 2006;33:216–224. [PubMed: 16485428]
19. Berard V, Rousseau JA, Cadorette J, Hubert L, Bentourkia M, van Lier JE, Lecomte R. Dynamic imaging of transient metabolic processes by small-animal PET for the evaluation of photo sensitizers in photodynamic therapy of cancer. J. Nucl. Med 2006;47:1119–1126. [PubMed: 16818946]
20. de Geus-Oei LF, Visser EP, Krabbe PFM, van Hoorn BA, Koenders EB, Willemsen AT, Pruim J, Corstens FHM, Oyen WJG. Comparison of image-derived and arterial input functions for estimating the rate of glucose metabolism in therapy-monitoring F-18-FDG PET studies. J. Nucl. Med 2006;47:945–949. [PubMed: 16741303]
21. Wahl RL, Quint LE, Greenough RL, Meyer CR, White RI, Orringer MB. Staging of Mediastinal Nonsmall Cell Lung-Cancer with FDG PET, CT, and Fusion Images—Preliminary Prospective Evaluation. Radiology 1994;191:371–377. [PubMed: 8153308]
22. Toyohara J, Hayashi A, Gogami A, Fujibayashi Y. Alkyl-fluorinated thymidine derivatives for imaging cell proliferation II. Synthesis and evaluation of N(3)-(2-[(18)F] fluoroethyl)-thymidine. Nucl. Med. Biol 2006;33:765–772. [PubMed: 16934695]
23. Yap CS, Czernin J, Fishbein MC, Cameron RB, Schiepers C, Phelps ME, Weber WA. Evaluation of thoracic tumors with 18F-fluorothymidine and 18F-fluorodeoxyglucose-positron emission tomography. Chest 2006;129:393–401. [PubMed: 16478857]
24. Jacobs AH, Thomas A, Kracht LW, Li HF, Dittmar C, Garlip G, Gaildiks N, Klein JC, Sobesky J, Hilker R, Vollmar S, Herholz K, Wienhard K, Heiss WD. F-18-fluoro-L-thymidine and C-11-methylmethionine as markers of increased transport and proliferation in brain tumors. J. Nucl. Med 2005;46:1948–1958. [PubMed: 16330557]
25. Installe J, Nzeusseu A, Bol A, Depresseux G, Devogelaer JP, Lonneux M. (18)F-fluoride PET for monitoring therapeutic response in Paget's disease of bone. J. Nucl. Med 2005;46:1650–1658. [PubMed: 16204715]
26. Brenner W, Vernon C, Conrad EU, Eary JF. Assessment of the metabolic activity of bone grafts with (18)F-fluoride PET. Eur. J. Nucl. Med. Mol. Imaging 2004;31:1291–1298. [PubMed: 15197502]
27. Segars WP, Tsui BMW, Frey EC, Johnson GA, Berr SS. Development of a 4-D digital mouse phantom for molecular imaging research. Mol. Imaging Biol 2004;6:149–159. [PubMed: 15193249]
28. Qi J, Leahy RM, Cherry SR, Chatziioannou A, Farquhar TH. High-resolution 3D Bayesian image reconstruction using the microPET small-animal scanner. Phys. Med. Biol 1998;43:1001–1013. [PubMed: 9572523]
29. Thie JA. Understanding the standardized uptake value, its methods, and implications for usage. J. Nucl. Med 2004;45:1431–1434. [PubMed: 15347707]
30. Leoning AM, Gambhir SS. AMIDE: a free software tool for multimodality medical image analysis. Mol. Imaging 2003;2:131–137. [PubMed: 14649056]
31. Fueger BJ, Czernin J, Hildebrandt I, Tran C, Halpern BS, Stout D, Phelps ME, Weber WA. Impact of animal handling on the results of 18F-FDG PET studies in mice. J. Nucl. Med 2006;47:999–1006. [PubMed: 16741310]
32. Jan S, et al. GATE: a simulation toolkit for PET and SPECT. Phys. Med. Biol 2004;49:4543–4561. [PubMed: 15552416]
33. Agostinelli S, et al. Geant4-a simulation toolkit. Nucl. Instrum. Methods Phys. Res. A 2003;506:250–303.
34. Baro J, Sempau J, Fernandez-Varea JM, Salvat F. PENELOPE: An algorithm for Monte Carlo simulation of the penetration and energy loss of electrons and positrons in matter. Nucl. Instrum. Methods Phys. Res. B 1995;100:31–46.
35. ICRU Report. Bethesda, MD: International Commission on Radiation Units and Measurements; 1992. Photon, electron, proton, and neutron interaction data for body tissues.

36. Levin CS, Hoffman EJ. Calculation of positron range and its effect on the fundamental limit of positron emission tomography system spatial resolution. Phys. Med. Biol 1999;44:781–799. [PubMed: 10211810]
37. Levin CS, Hoffman EJ. Calculation of positron range and its effect on the fundamental limit of positron emission tomography system spatial resolution (vol. 44, pg 781, 1999). Phys. Med. Biol 2000;45 559–559.
38. Thomas SR, Stabin MG, Chen CT, Samaratunga RC. MIRD Pamphlet No. 14 revised: A dynamic urinary bladder model for radiation dose calculations. J. Nucl. Med 1999;40:102S–123S. [PubMed: 10210232]
39. Stabin MG, Siegel JA, Sparks RB, Eckerman KF, Breit HB. Contribution to red marrow absorbed dose from total body activity: A correction to the MIRD method. J. Nucl. Med 2001;42:492–498. [PubMed: 11337528]
40. Hays MT, Watson EE, Thomas SR, Stabin M. MIRD dose estimate report No. 19: Radiation absorbed dose estimates from F-18-FDG. J. Nucl. Med 2002;43:210–214. [PubMed: 11850487]
41. Eckerman KF, Stabin MG. Electron absorbed fractions and dose conversion factors for marrow and bone by skeletal regions. Health Phys 2000;78:199–214. [PubMed: 10647986]
42. Nose M, Wang B, Itsukaichi H, Yukawa O, Hayata I, Yamada T, Ohyama H. Rescue of lethally irradiated mice from hematopoietic death by pre-exposure to 0.5 Gy X rays without recovery from peripheral blood cell depletion and its modification by OK432. Radiat. Res 2001;156:195–204. [PubMed: 11448241]
43. Hall, EJ. Radiobiology for the Radiologist. 4th ed.. Philadelphia: Lippincott; 1994.
44. Wang GJ, Cai L. Induction of cell-proliferation hormesis and cell-survival adaptive response in mouse hematopoietic cells by whole-body low-dose radiation. Toxicol. Sci 2000;53:369–376. [PubMed: 10696785]
45. Yonezawa M. Induction of radio-resistance by low dose X-irradiation. Yakugaku Zasshi 2006;126:833–840. [PubMed: 17016014]

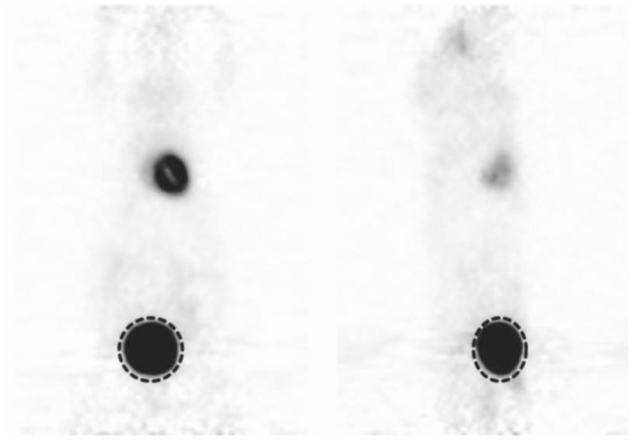

(a)

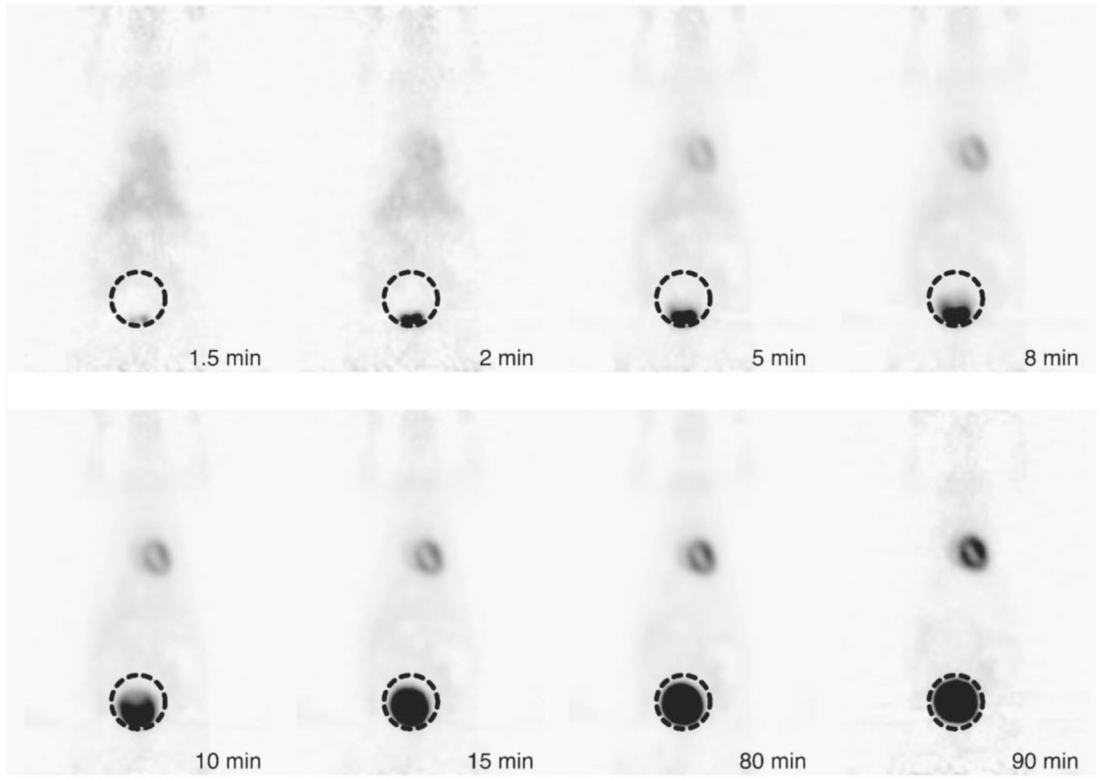

(b)

FIG. 1.

(a) Coronal (left) and sagittal (right) views of the time-integrated image of the ^{18}FDG study with an ellipsoid region of interest has been drawn around the bladder. (b) Selected frames showing the bladder ROI at a fixed position as activity accumulates with time (time increases from left to right and top to bottom).

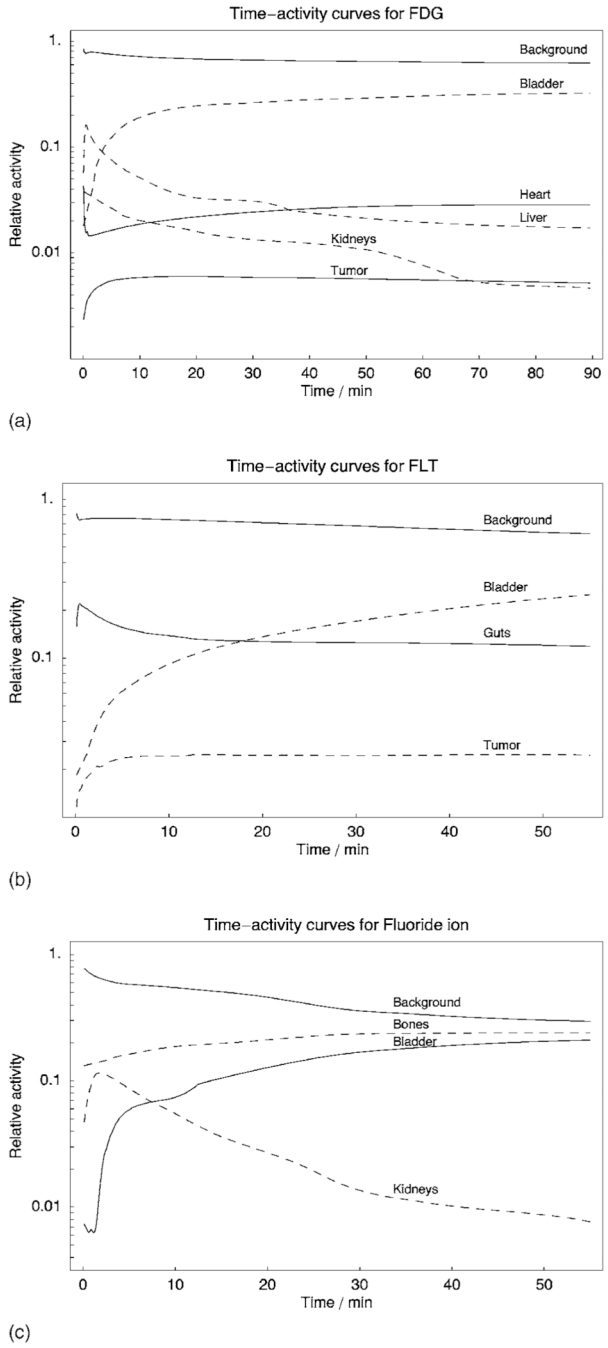

FIG. 2.

Time-activity curves extracted from PET studies plotted as cubicspline interpolations from data points: (a) ^{18}FDG, (b) ^{18}FLT, and (c) [^{18}F]fluoride ion.

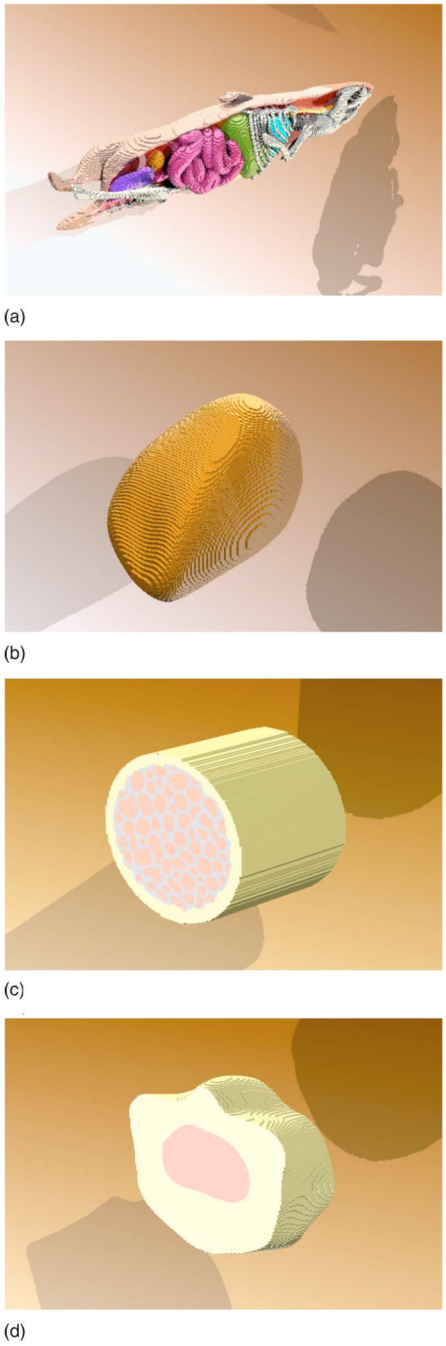

FIG. 3.
Phantoms used in this study: (a) a voxelized realization (400 μm) of the whole-mouse MOBY phantom, (b) the high-resolution bladder phantom (50 μm), (c) the high-resolution femur head model (15 μm), and (d) the high-resolution vertebra (25 μm).

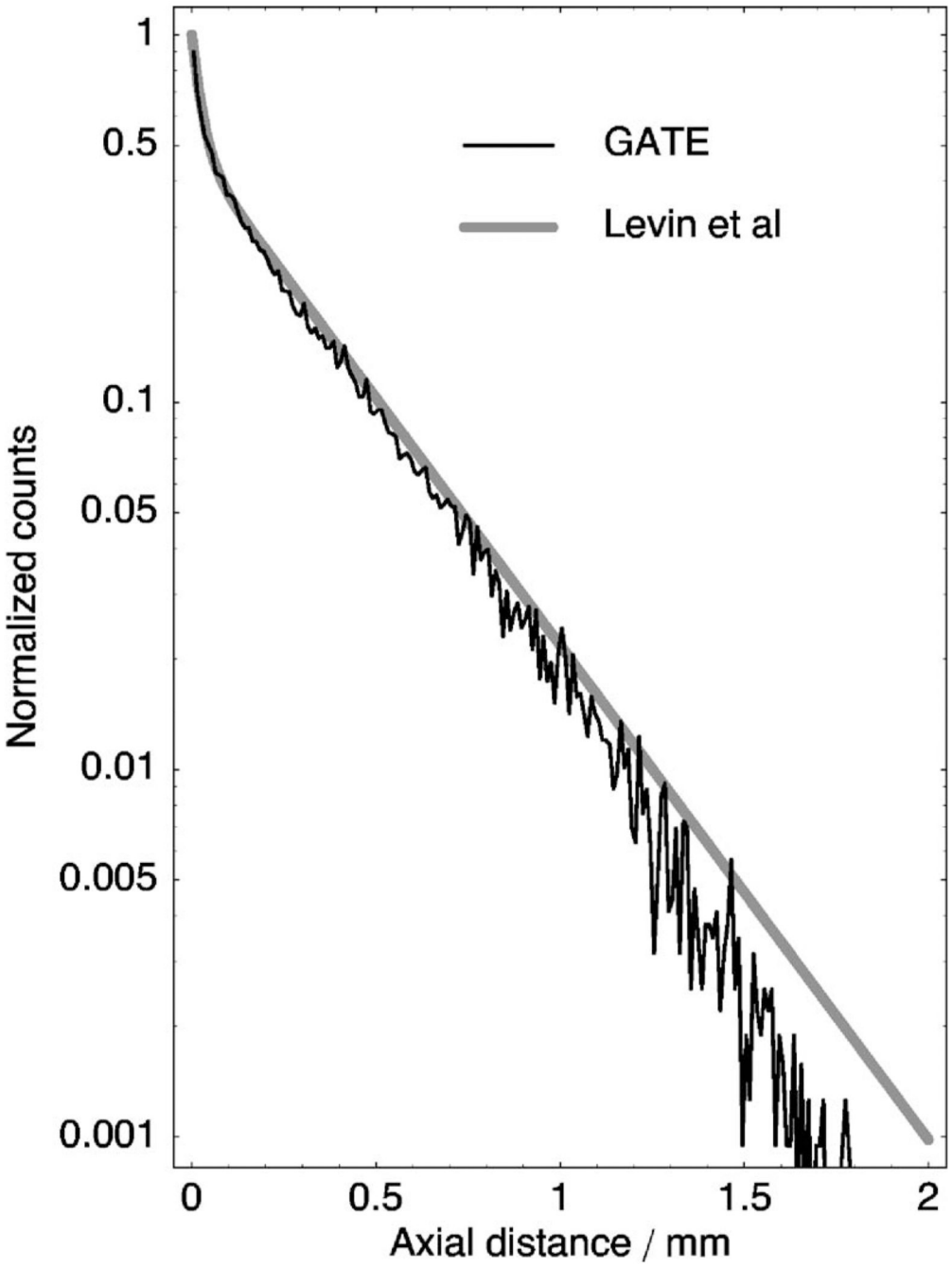

FIG. 4.

Comparison of the *x*-coordinate distribution of positron annihilation points in water as calculated by GATE and by Levin and Hoffman[36] as a bi-exponential function: $q(x)=C/e^{-k1x}+(1-C)e^{-k2x}$ with C=0.516, $k1$=37.90, and $k2$=3.1.

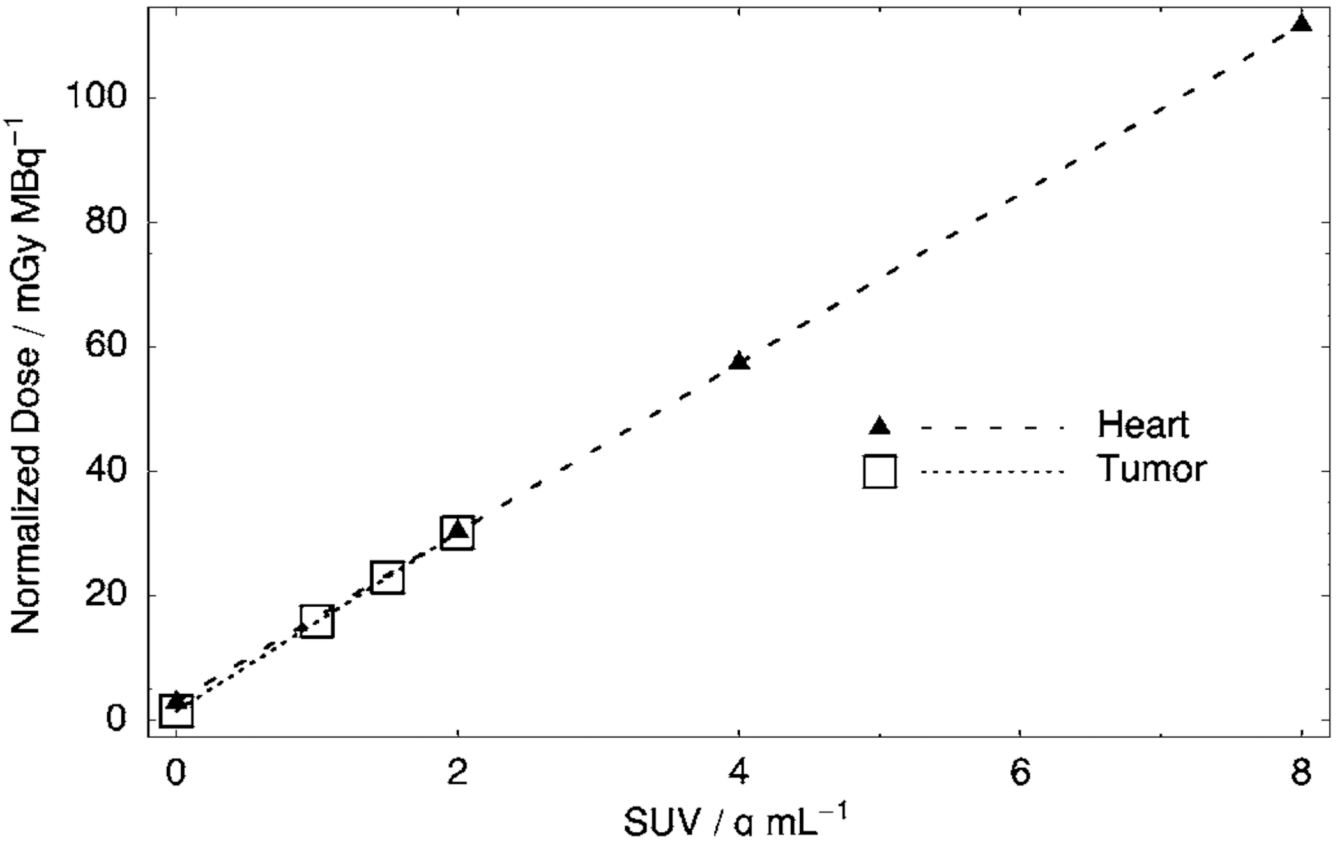

FIG. 5.
Plot of normalized absorbed dose for heart and tumor as a function of SUV.

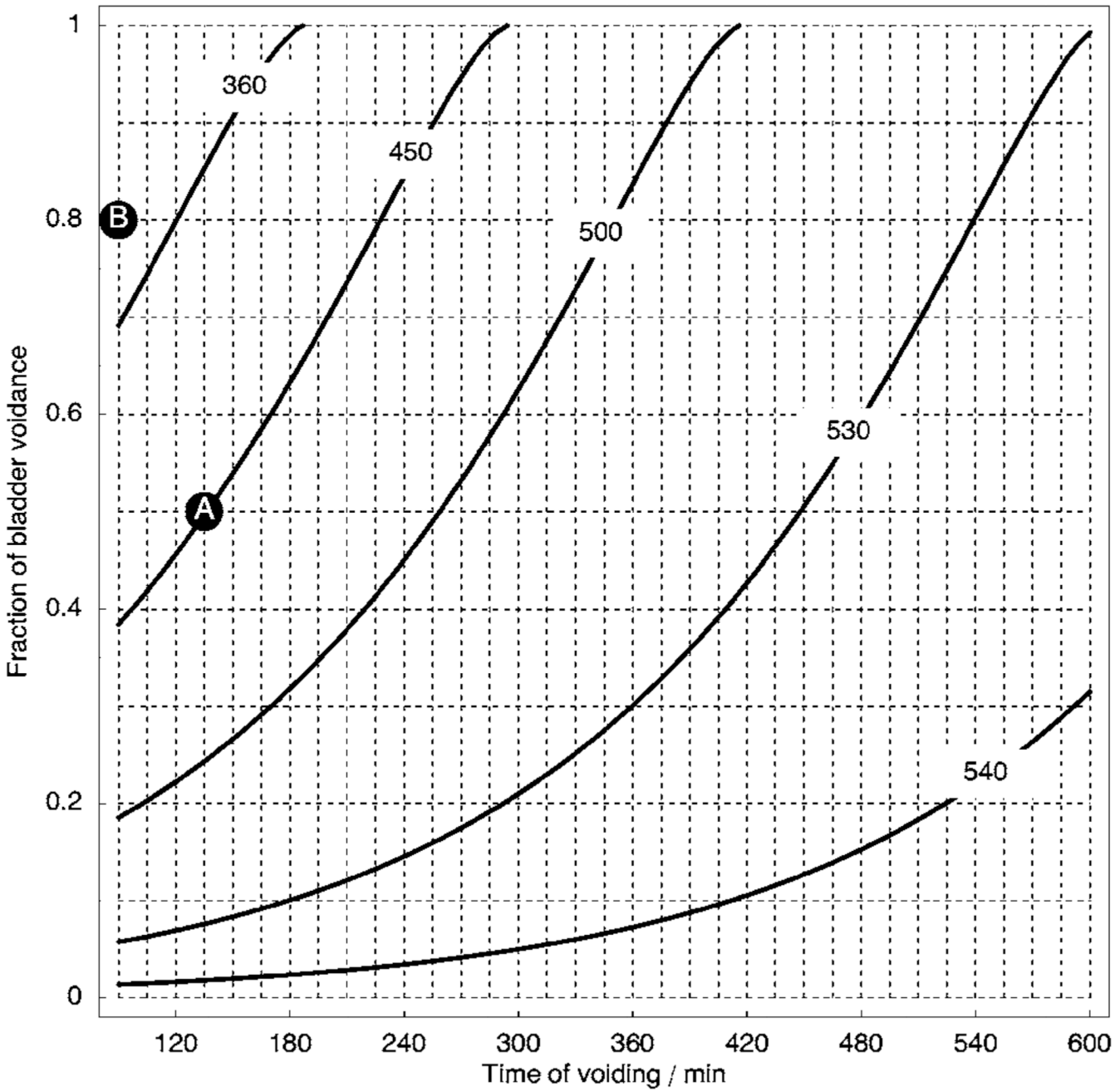

FIG. 6.

Normalized isodose map (mGy/MBq) for the bladder wall in an ^{18}FDG study as a function of the time and amount of bladder voidance. The time is given in minutes following injection and voidance is expressed as a fraction between 0 (full bladder) and 1 (empty bladder).

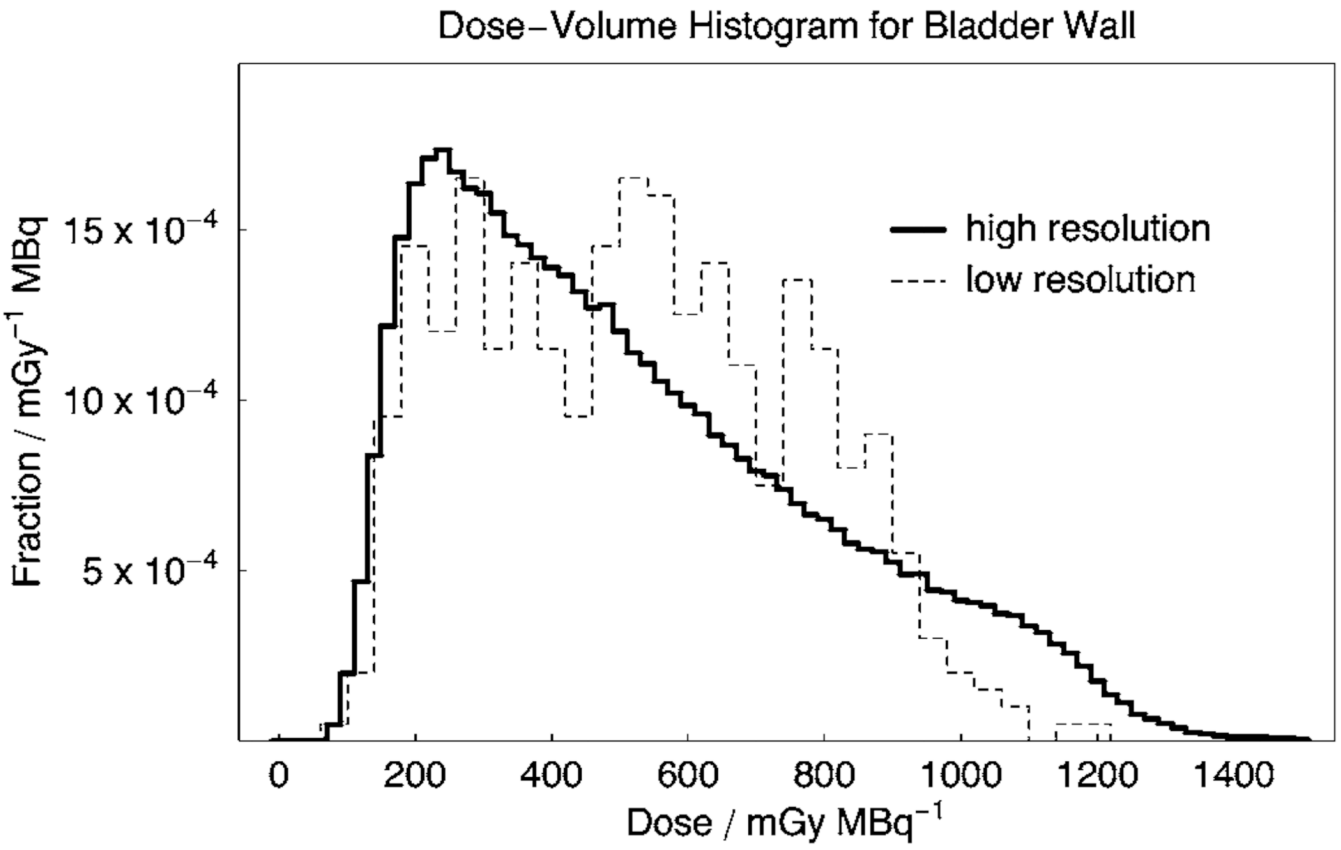

FIG. 7.

Comparative dose-volume histograms for the bladder wall obtained with the high- and low-resolution phantoms. The average doses were 529 and 543 mGy for the high- and low-resolution phantom, respectively.

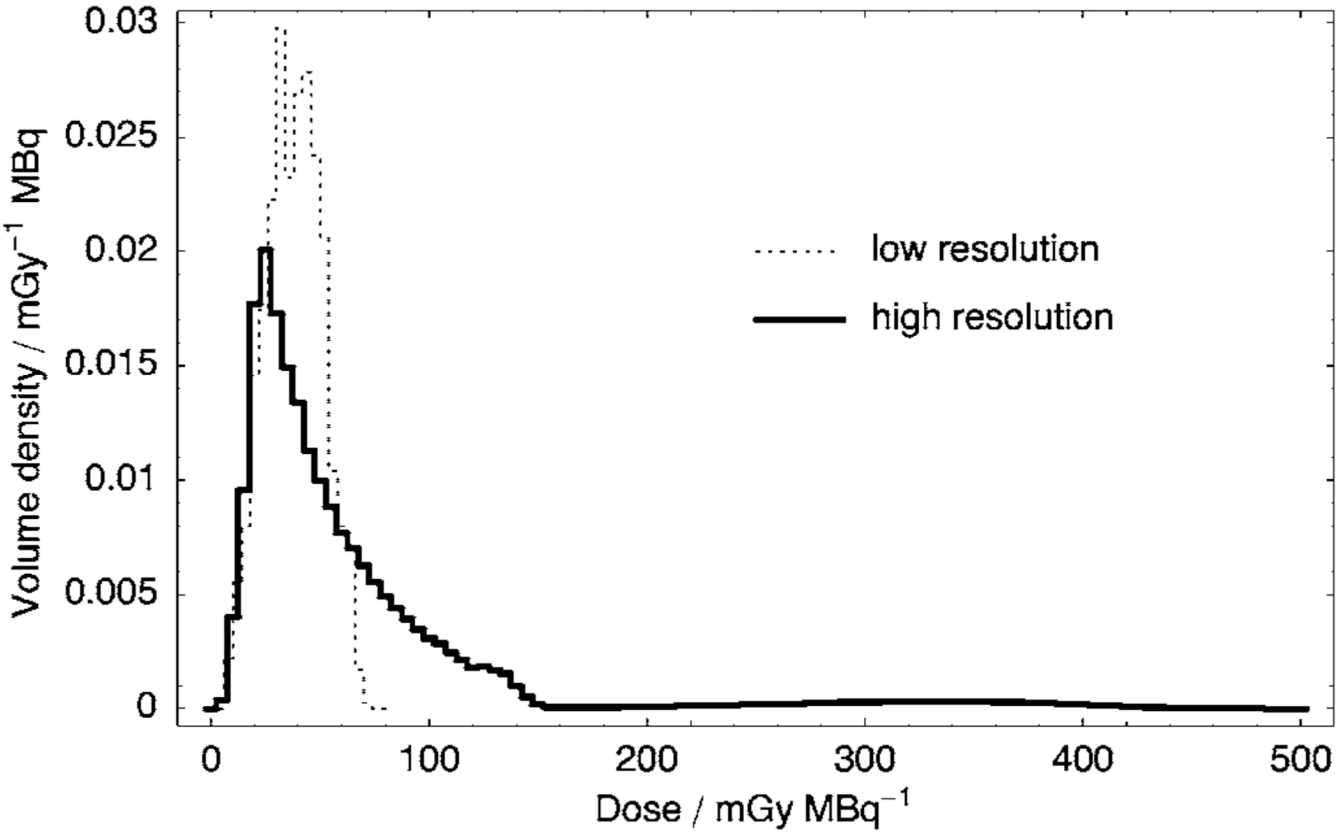

FIG. 8.
Dose-volume histogram for the bone marrow calculated with the low-resolution whole-mouse phantom, and two-high-resolution bone phantoms: vertebra and femur head.

TABLE I

Calculated absorbed dose in selected organs/structures from ^{18}FDG, ^{18}FDG, and [^{18}F]fluoride ion simulations normalized per MBq administered activity.

Structure name	Mass (mg)	FDG (mGy/MBq)	FLT (mGy/MBq)	Fluoride ion (mGy/MBq)
Bladder wall (low-res)	45	543	423	342
Bladder wall (hi-res)	···	529	412	333
Body mass	16 730	14	13	10
Brain	635	13	12	13
Cranium	570	4	4	62
Heart	120	3+13.6*SUV	13	8
Intestine wall	1820	4	11	3
Kidneys	415	26	14	16
Lower limbs	615	3	3	64
Liver	2690	6	13	8
Lungs	130	9	6	11
Pancreas	440	14	13	8
Ribs	673	5	5	28
Skin	6910	3	2	3
Bone (spine)	645	5	4	76
Marrow (low-res)	70	10	9	41
Marrow (hi-res)	···	···	···	66
Spleen	130	13	12	7
Stomach wall	85	4	5	4
Testes	400	16	14	9
Thyroid	15	14	13	5
Tumor	15	1.5+14.3*SUV	66	···
Vas deferens	30	30	24	18

TABLE II

Calculated absorbed dose for a 7.4 MBq injection.

Structure name	FDG (mGy/ 7.4 MBq)	FLT (mGy/ 7.4 MBq)	Fluoride ion (mGy/ 7.4 MBq)
Bladder wall (low-res)	4018	3130	2531
Bladder wall (hi-res)	3915	3050	2466
Body	106	96	77
Brain	98	89	94
Cranium	30	30	457
Heart	425	96	61
Intestine wall	29	81	19
Kidneys	195	104	117
Lower limbs	26	22	473
Liver	42	95	58
Lungs	67	44	79
Pancreas	100	96	56
Ribs	38	35	206
Skin	19	18	21
Bone (spine)	36	32	560
Marrow (low-res)	74	67	306
Marrow (hi-res)	…	…	488
Spleen	96	88	52
Stomach wall	32	37	26
Testes	118	106	64
Thyroid	105	95	37
Tumor	223	488	…
Vas deferens	221	181	136